

# Realization and simulation of interdigitated back contact silicon solar cells with dopant-free asymmetric hetero-contacts

Wenjie Wang<sup>a,b</sup>, Jian He<sup>b,c</sup>, Di Yan<sup>d</sup>, Wenhao Chen<sup>b,e</sup>, Sieu Pheng Phang<sup>b</sup>,  
Christian Samundsett<sup>b</sup>, Siva Krishna Karuturi<sup>b</sup>, Zhengping Li<sup>a</sup>, Yimao Wan<sup>b,f</sup>,  
Wenzhong Shen<sup>a,\*</sup>

<sup>a</sup> Key Laboratory of Artificial Structures and Quantum Control (Ministry of Education), Institute of Solar Energy, School of Physics and Astronomy, Shanghai Jiao Tong University, Shanghai 200240, China

<sup>b</sup> School of Engineering, The Australian National University, Canberra, ACT 2601, Australia

<sup>c</sup> School of Materials, Sun Yat-sen University, Guangzhou 510275, China

<sup>d</sup> School of Electrical and Electronic Engineering, University of Melbourne, Melbourne, VIC 3052, Australia

<sup>e</sup> School of Testing and Photoelectric Engineering, Nanchang Hang Kong University, Nanchang 330063, PR China

<sup>f</sup> Center of Cell Research, Risen Energy Co., Ltd., Ningbo 315609, China

## ARTICLE INFO

### Keywords:

Back contact c-Si solar cells  
Dopant-free  
Surface passivation  
Contact resistivity  
Quokka 2 simulation

## ABSTRACT

Crystalline silicon (c-Si) solar cells using interdigitated back contact (IBC) configurations are one of the most promising candidates to reach the practical efficiency limits of c-Si solar cells. However, the complexity of the process flow hinders the mass production of the IBC cells with conventional doped regions. One of the simple fabrication methods is to introduce the dopant-free carrier-selective contacts, which utilizes the fabrication processes with low temperature, e.g., the thermal evaporation or the spin coating. In this paper, we investigated efficiency close to 20% silicon IBC solar cells with dopant-free asymmetric hetero-contacts. In this solar cell configuration, the high work function material MoO<sub>x</sub> was chosen as the hole transporting layer, while the low work function material LiF was chosen as the electron transporting layer, respectively. The simulation results indicate that the perspective efficiency exceeding 22% for this type of cells is achievable with the optimized pitch width and improved passivation quality of the contacts, which has a great potential for the industrialization of IBC solar cells with simple fabrication processes.

## 1. Introduction

Recently, crystalline silicon (c-Si) solar cells based on interdigitated back contact (IBC) configurations have succeeded in achieving the world-record power conversion efficiency (PCE) of 26.7% with the silicon heterojunction (SHJ) technology (Yoshikawa et al., 2017a). The structure takes advantages of eliminating the optical loss by completely avoiding front-side metal grids shading and excellent surface passivation qualities obtained from hydrogenated intrinsic amorphous silicon (a-Si:H(i)) films. This leads to silicon solar cells with high short-circuit current density ( $J_{sc} > 41 \text{ mA/cm}^2$ ) and high open-circuit voltages ( $V_{oc} > 700 \text{ mV}$ ) (Yoshikawa et al., 2017a; Yoshikawa et al., 2017b). However, it is a tough challenge to have mass production of this type of IBC solar cells due to their complex fabrication process flow. For example, multiple photolithographic patterning processes are required to identify rear side

regions with phosphorus and boron-doped a-Si:H films, which are formed by dangerous and toxic gas precursors (e.g., PH<sub>3</sub>). In addition, the phosphorus and boron-doped a-Si:H films, as the electron transporting layer (ETL) and hole transporting layer (HTL) for the IBC cells, respectively, also restrain the further promotion on the theoretical limiting efficiency of 29.4% due to the parasitic electrical and optical loss (Richter and Glunz, 2013). Therefore, the further improvement would be realized by simplifying the cells process flow and seeking for new materials to replace the doped layers. One of the promising solutions to overcome these barriers is to introduce dopant-free carrier-selective contacts.

Dopant-free carrier-selective contacts which are formed by either low or high work function materials greatly attract researchers' interest in fabricating high-efficiency silicon solar cells. These materials can extract one type of carrier (holes or electrons) while block the others via

\* Corresponding author.

E-mail addresses: [hejian7@mail.sysu.edu.cn](mailto:hejian7@mail.sysu.edu.cn) (J. He), [wzshen@sjtu.edu.cn](mailto:wzshen@sjtu.edu.cn) (W. Shen).

<https://doi.org/10.1016/j.solener.2021.11.044>

Received 23 August 2021; Received in revised form 1 November 2021; Accepted 15 November 2021  
0038-092X/© 2021 International Solar Energy Society. Published by Elsevier Ltd. All rights reserved.

band offsets, which functions similarly as either n-type or p-type doped silicon regions in silicon solar cells (Melskens et al., 2018). These functional materials often have a wide band gap, effectively avoiding the optical parasitic absorption. Additionally, they can be easily deposited by the simple low-temperature thermal evaporation or the spin coating without involving any toxic dopants and high temperature processes. So far, high work function materials (above 6.5 eV in the ideal case) (Allen et al., 2019), such as transition metal oxides (e.g., molybdenum oxide (Bullock et al., 2014; Battaglia et al., 2014; Dréon et al., 2020), tungsten oxide (Bivour et al., 2015), and vanadium oxide (Almora et al., 2017a, 2017b; Yang et al., 2020a, 2020b)), organic polymer (e.g., poly(3,4-ethylene dioxothiophene): poly(styrenesulfonate) (He et al., 2018), and poly(3-hexylthiophene) (Freitas et al., 2014), low dimensional carbon materials (e.g., carbon nanotube (Xu et al., 2018) and graphene (Tune et al., 2012)) have been successfully used as HTL while low work function materials (lower than about 4 eV) (Melskens et al., 2018), such as some metal oxides (e.g., titanium oxide (Yang et al., 2016; Yang et al., 2017), magnesium oxide (Wan et al., 2017a; Yu et al., 2019), and tantalum oxide (Yang et al., 2018)), metal nitrides (e.g., titanium nitride (Yang et al., 2019), titanium oxynitride (Yang et al., 2020a, 2020b) and tantalum nitride (Yang et al., 2020a, 2020b)), metal fluorides (e.g., lithium fluoride (Bullock et al., 2016) and magnesium fluoride (Wan et al., 2017b)), metal carbonates (e.g., cesium carbonate, potassium carbonate, and calcium carbonate (Wan et al., 2018)), low work function metals (e.g., calcium (Allen et al., 2017) and magnesium (Wan et al., 2016a, 2016b)) have been demonstrated as ETL. Furthermore, silicon solar cells with dopant-free asymmetric hetero-contacts also have been reported in recent years. The silicon solar cells with efficiency of 20.7% using high-quality passivating a-Si:H(i) films, MoO<sub>x</sub>/Ag as HTL and TiO<sub>x</sub>/LiF/Al as ETL (Bullock et al., 2018), and efficiency of 21.4% using alternative ZnO/LiF/Al as ETL have been demonstrated (Zhong et al., 2019). As for IBC structure, the efficiency of 20.1% has been reported using passivating a-Si:H(i) films, MoO<sub>x</sub>/Ag as HTL and LiF/Al as ETL (Wang et al., 2019). A higher efficiency of 22.1% was reported by using optimized double antireflective layers SiN<sub>x</sub>/MgF<sub>x</sub> to enhance the optical absorption and dopant-free electron transporting multilayers MgF<sub>x</sub>/Mg/Al to lower the contact resistivity (Wu et al., 2020).

In this paper, we experimentally demonstrated IBC c-Si solar cells with the efficiency with 19.4%. The cells are composed of dopant-free asymmetric hetero-contacts, using high work functional MoO<sub>x</sub>/Ag contact as HTL and low work functional LiF/Al contact as ETL. The whole device was completed within five steps. The electrical properties including both passivation qualities and contact resistivities of HTL with different a-Si:H(i) thicknesses were studied. Finally, Quokka 2 simulation software was employed to seek the optimized pitch width and passivation quality of the contacts and assist us to understand the efficiency limitations of our current cell designs for achieving high

efficiency devices in future.

## 2. Results and discussion

Fig. 1(a) illustrates the schematic of the dopant-free IBC c-Si solar cells. The processing flow of our dopant-free IBC c-Si solar cell was shown in Fig. 1(b). The cell substrates used for cells fabrication were Cz n-type c-Si wafers with the bulk resistivity of 1 Ωcm and a thickness of 200 μm. After a series of wet chemical process, including alkaline saw damage polish, single-side random-pyramids texture and standard RCA cleaning, the passivation and antireflection SiN<sub>x</sub> layer with a thickness of 75 nm was deposited on the front side by plasma-enhanced chemical vapor deposition (PECVD) technology. The passivation quality and optical property of PECVD SiN<sub>x</sub> was reported in reference (Wan et al., 2013). For the rear side, hydrogenated intrinsic amorphous silicon (a-Si:H(i)) film with the optimized thickness (5 nm) deposited by PECVD was used as the passivating layer. Evaporated MoO<sub>x</sub>/Ag stack (8 nm/300 nm) and LiF/Al stack (1 nm/300 nm) were patterned by using shadow masks, which were used as the HTL and ETL for IBC cells, respectively.

The key success to achieve a high efficiency c-Si solar cell is to have well passivated silicon surfaces that maximize the generated carrier concentrations in the silicon. One is to use the a-Si:H(i) films as the surface passivating layer in the c-Si solar cells, which has been successfully implemented in the SHJ solar cells with world recorded efficiencies. (Yoshikawa et al., 2017a,b) Although the recombination at the c-Si/HTL or c-Si/ETL interface can be significantly suppressed by introducing the a-Si:H(i) passivating layer, their correspondent contact resistivities can be high due to the high bulk resistivity of a-Si:H(i) layer. Thus, it is critical to optimize the thickness of a-Si:H(i) to achieve both excellent passivation quality and low contact resistivities. Fig. 2(a) presents the surface passivation quality formed by both-sides a-Si:H(i) layers (red curve), as well as their correspondent contact resistivity ρ<sub>c</sub> (blue curves) with 1 nm LiF/100 nm Al and 8 nm MoO<sub>x</sub>/100 nm Ag as a function of a-Si:H(i) thickness. As can be seen, the 3 nm a-Si:H(i) layer provides relatively poor surface passivation, which has an implied V<sub>OC</sub> of 653 mV. However, the implied V<sub>OC</sub> value can be improved dramatically from 653 mV to 719 mV by using slightly thicker 4 nm a-Si films. The passivation quality saturates at iV<sub>OC</sub> of over 720 mV for a-Si:H(i) thickness over 4 nm. On the other hand, as increasing a-Si:H(i) thickness increasing from 3 nm to 7 nm, the contact resistivity ρ<sub>c</sub> increases from 34.4 to 223.6 mΩcm<sup>2</sup> for HTL with a structure of a-Si:H(i)/8 nm MoO<sub>x</sub>/100 nm Ag contact, while the contact resistivity ρ<sub>c</sub> values of ETL with a structure of a-Si:H(i)/1 nm LiF/100 nm Al increases from 24.1 to 82.6 mΩcm<sup>2</sup>. Since there is a large impact on the HTL rather than ETL, we further explored the contact resistivity of HTL as a function of MoO<sub>x</sub> thickness, as indicated in Fig. 2(b). The contact resistivity ρ<sub>c</sub> of a-Si:H(i)/MoO<sub>x</sub>/Ag increases tenderly below 8 nm and performs unacceptably

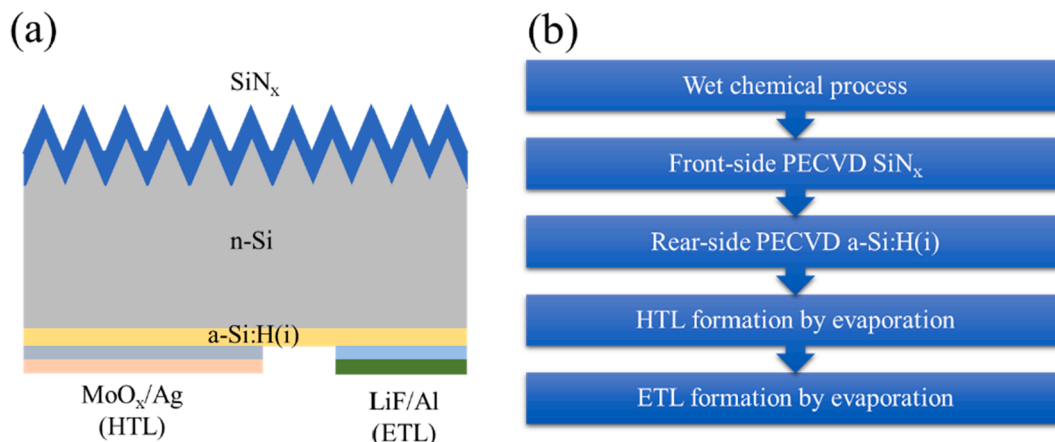
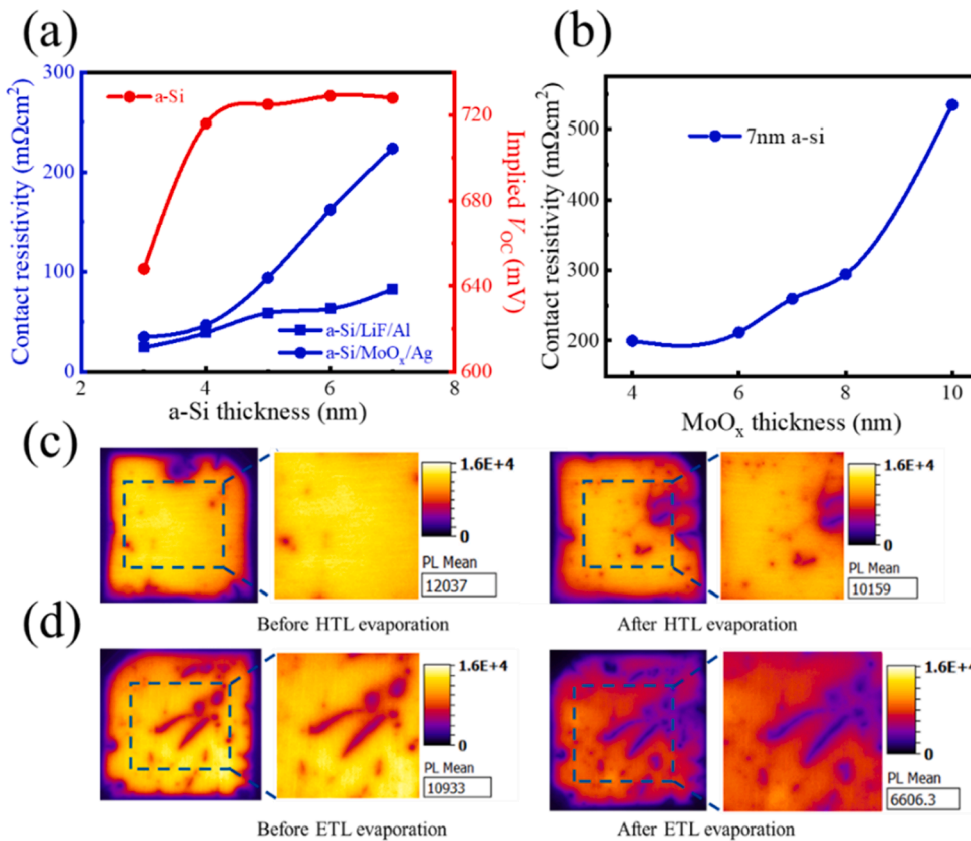


Fig. 1. (a) Schematic of the dopant-free IBC silicon solar cells and (b) the process flow for the cells.



**Fig. 2.** (a) Implied open circuit voltage  $iV_{OC}$  (red curve) of a-Si:H(i) and contact resistivity  $\rho_c$  (blue curves) of a-Si/LiF/Al and a-Si/MoO<sub>x</sub>/Ag structures as a function of a-Si:H(i) thickness. (b) Contact resistivity  $\rho_c$  of MoO<sub>x</sub>/Ag as a function of MoO<sub>x</sub> thickness. PL images of (c) the a-Si:H(i) passivated samples before (left) and after (right) MoO<sub>x</sub>/Ag evaporation (d) a-Si:H(i) passivated samples before (left) and after (right) LiF/Al evaporation. The PL images were captured at an illumination intensity of 0.5 suns. (For interpretation of the references to colour in this figure legend, the reader is referred to the web version of this article.)

high value over 500 mΩcm<sup>2</sup> when the MoO<sub>x</sub> thickness reaches to 10 nm due to the low conductivity of the bulk MoO<sub>x</sub>, as reported in reference (Dréon et al., 2020). Based on those results, a thickness of 5 nm a-Si:H(i) layer and 8 nm MoO<sub>x</sub> have been chosen for the solar cells fabrication.

To evaluate the passivation quality and the uniformity of both HTL and ETL structures after metal evaporation, the photoluminescence (PL) images were used. Fig. 2(c) presents the PL images of silicon substrates with the both side 5 nm a-Si:H(i) passivating layers before (left) and after (right) single side 8 nm MoO<sub>x</sub>/100 nm Ag evaporation while Fig. 2(d) shows the PL intensities of the PL images of silicon substrates with the both side 5 nm a-Si:H(i) passivating layers before (left) and after (right) single side 1 nm LiF/100 nm Al evaporation, respectively. As can be seen, the passivation quality maintains a high level after MoO<sub>x</sub>/Ag evaporation while the degradation has been observed after LiF/Al evaporation. The most likely reason for the degradation of the passivation might ascribe to the direct contact of a-Si:H(i) passivating film and Al due to the ultrathin LiF film.

A well-designed pitch width for contacts is necessary to realize high efficiency IBC solar cells. To explore the suitable width of the pitch, Quokka 2 software was employed to seek optimized pitch sizes. In this case, in order to ensure the hard-mask process stability and avoid the metal electrodes contact between HTL and ETL patterns during the process, the gap width was fixed to 150 μm. Table 1 lists the simulation parameters of the IBC cells, which were obtained from tested samples as discussed in the previous sections. Fig. 3 shows the (a) open-circuit voltage ( $V_{OC}$ ), (b) short-circuit current density ( $J_{SC}$ ), (c) fill factor (FF), and (d) power conversion efficiency (PCE) of the solar cells with different widths of HTL and ETL contacts, which have a range from 100 μm to 800 μm. It showed that the  $V_{OC}$  is less affected since excellent passivation have been provided by front side SiN<sub>x</sub> and rear side a-Si:H(i) passivating layer. The simulation results indicate that  $V_{OC}$  would vary from 719 mV to 723 mV and there are no significant changes which have been observed by varying the HTL and ETL regions. The observation of

**Table 1**

Main parameter values for the Quokka 2 simulations.

Quokka 2 parameters	
Bulk resistivity (Ωcm)	1
Wafer thickness (μm)	230
Background lifetime (ms)	5
Front passivation $J_0$ (fA/cm <sup>2</sup> )	7
HTL passivation $J_0$ (fA/cm <sup>2</sup> )	10
Gap passivation $J_0$ (fA/cm <sup>2</sup> )	4.3
ETL passivation $J_0$ (fA/cm <sup>2</sup> )	15
HTL contact resistivity $\rho$ (mΩcm <sup>2</sup> )	200
ETL contact resistivity $\rho$ (mΩcm <sup>2</sup> )	40

the  $J_{SC}$  with different pitch widths of HTL and ETL in Fig. 3(b) reveals that a high  $J_{SC}$  value of over 41 mA/cm<sup>2</sup> can be realized with high HTL/ETL width ratio. In addition, ETL width larger than 300 μm would reduce the value of  $J_{SC}$ . The value of FF is determined by the width of HTL, as observed in Fig. 3(c), which indicates that a large HTL width (>400 μm) ensures the effective collection of holes in the HTL regions. Fig. 3(d) depicts the efficiency of the simulated IBC cells, providing the efficiency contour line with different width of HTL and ETL, which suggests the proper pitch width of both contacts for the dopant-free IBC solar cells could achieve the power conversion efficiency over 22%. A large enough HTL pitch width (over 400 μm) and a relatively small ETL pitch width (below 300 μm) are required for high-performance solar cells. Above all, the pitch widths of 750 μm for HTL, 150 μm for gap, and 250 μm for ETL were chosen for the following solar cell process.

To further consider the passivation effects of HTL and ETL contacts on photovoltaic parameters, the major parameters  $V_{OC}$  and  $J_{SC}$  of the solar cells were simulated as a function of recombination saturation parameter  $J_0$ , as indicated in Fig. 4, with other simulation parameters fixed as shown in Table 1. As depicted in Fig. 4(a), the  $V_{OC}$  would significantly decrease from 723 mV to 670 mV when the recombination

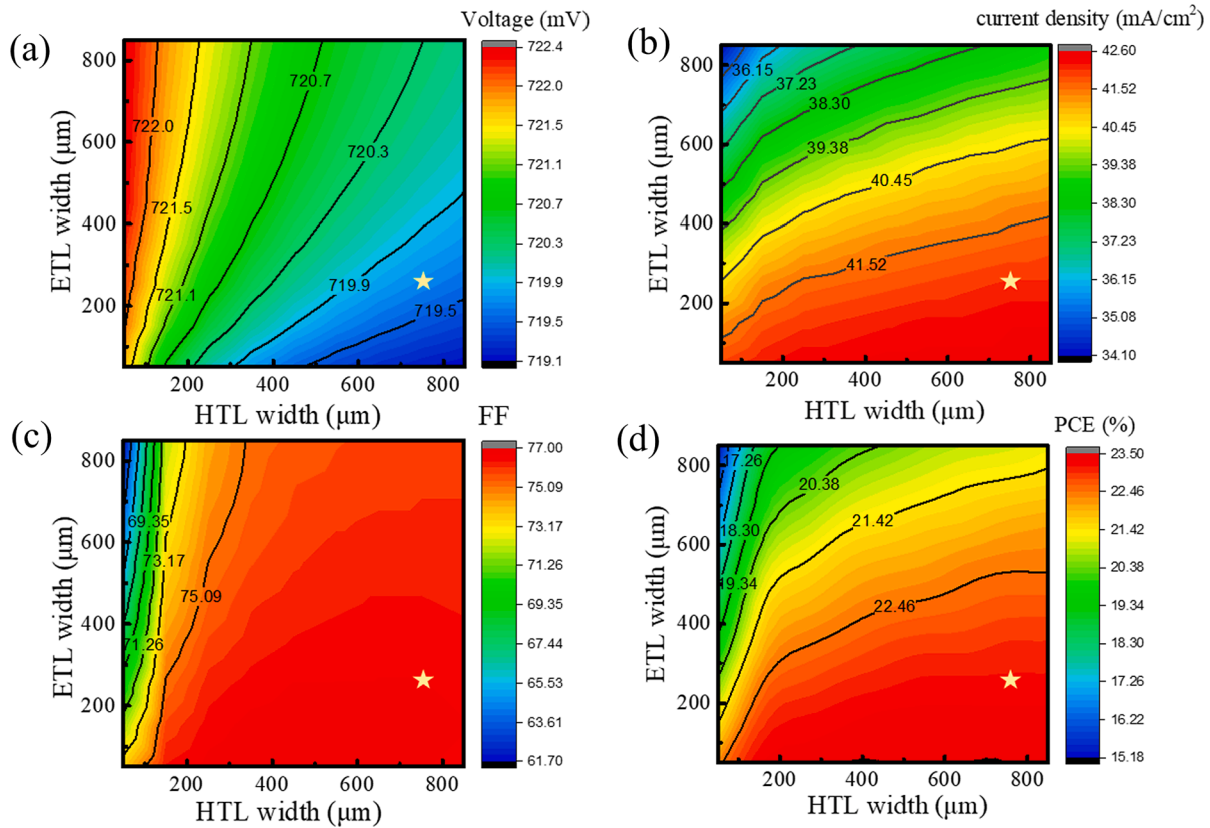


**Fig. 3.** Simulated electrical performance (a) open voltage ( $V_{OC}$ ), (b) short current density ( $J_{SC}$ ), (c) fill factor (FF), (d) power conversion efficiency (PCE) with different widths of HTL and ETL under the condition of the fixed 150  $\mu\text{m}$  gap by Quokka 2. The yellow stars show the experimental results in Fig. 5 with the pitch width of 750  $\mu\text{m}$  for HTL and 250  $\mu\text{m}$  for ETL. (For interpretation of the references to colour in this figure legend, the reader is referred to the web version of this article.)

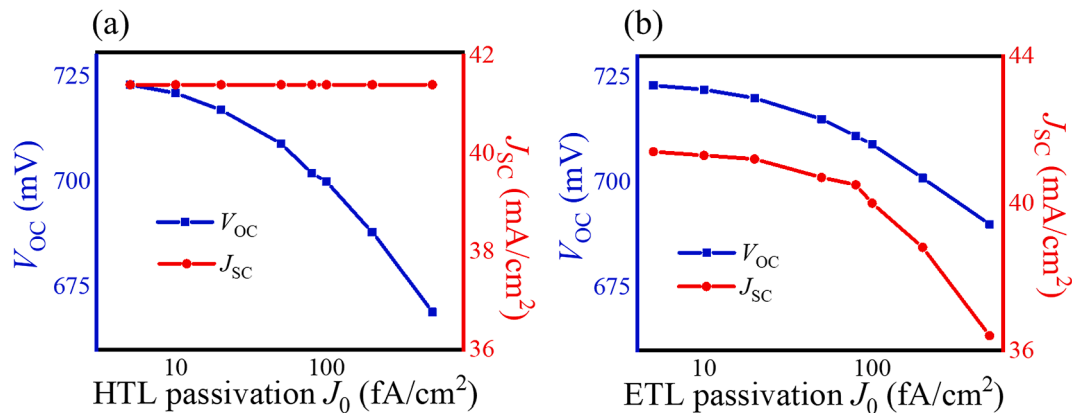


**Fig. 4.** Dependence on the recombination saturation parameter  $J_0$  of (a) HTL with the fixed  $J_0 = 10 \text{ fA/cm}^2$  at ETL and (b) ETL with the fixed  $J_0 = 15 \text{ fA/cm}^2$  at HTL and electrical parameters  $V_{OC}$  (blue curve) and  $J_{SC}$  (red curve). (For interpretation of the references to colour in this figure legend, the reader is referred to the web version of this article.)

saturation parameter  $J_0$  decreases from 5  $\text{fA/cm}^2$  to 500  $\text{fA/cm}^2$ . It is mainly because HTL has a larger area fraction than that of ETL. However, the  $J_{SC}$  of the cells would not change with the degradation of the passivation. For ETL regions, the better passivation indicates a higher  $J_{SC}$  and  $V_{OC}$ , which indicates the passivation quality influences the electron collection on the IBC cell. Although the pitch width of the ETL is less than the width of the HTL, the passivation of the ETL would have same effect as that of HTL due to the additional influence on the  $J_{SC}$ . The degradation of the  $J_{SC}$  reflects that the electron collection is influenced by high recombination in ETL region. Once the recombination

saturation parameter  $J_0$  increases over 100  $\text{fA/cm}^2$ , the  $J_{SC}$  would drop to lower than 40  $\text{mA/cm}^2$  in this case. The main reason for the passivation degradation is because the majority carriers in n-type silicon are electrons. The photogenerated holes near the ETL regions can easily recombine with the electrons, having a negative impact on carrier collection near the ETL regions.

Fig. 5(a) displayed the rear side of the actual device with the width 750  $\mu\text{m}$ , 150  $\mu\text{m}$ , and 250  $\mu\text{m}$  for the HTL, gap, and ETL, respectively. Fig. 5(b) presented the light current density–voltage ( $J$ - $V$ ) characteristics of the dopant-free IBC solar cell under standard AM 1.5 illumination

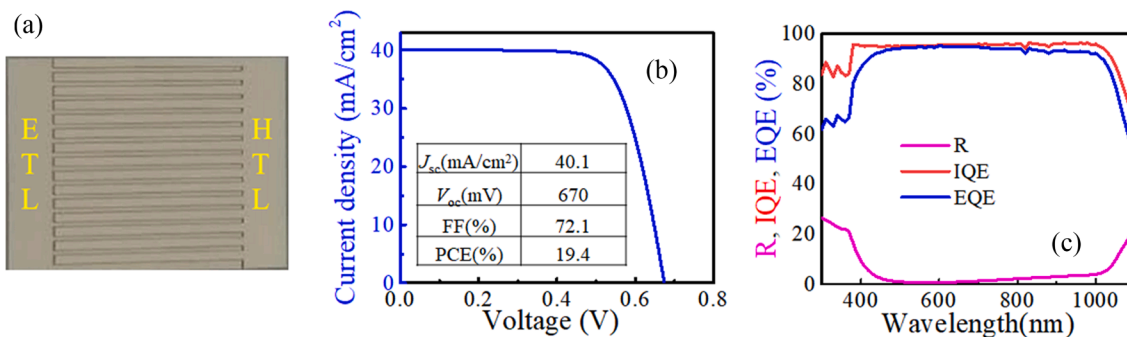


Fig. 5. (a) Optical image of the rear side of the IBC solar cell. (b) Light  $J$ - $V$  characteristics and electrical parameters of the dopant-free IBC solar cell under standard AM 1.5 illumination. (c) External quantum efficiency (EQE), internal quantum efficiency (IQE) and reflectance (R) of the solar cell.

with a power conversion efficiency of 19.4%, associated with the  $V_{OC}$ ,  $J_{SC}$ , and FF values of 670 mV, 40.1 mA/cm<sup>2</sup>, and 72.1%, respectively. Fig. 5(c) exhibited the corresponding quantum efficiency analysis including the external quantum efficiency (EQE), internal quantum efficiency (IQE) and reflectance (R) for the solar cell. As can be seen, the actual  $V_{OC}$  of 670 mV is further lower than the simulated results (700 mV), as shown the star in the Fig. 3(a). The main reason for the difference between the simulated results and experimental data (stars in Fig. 3) might be the passivation degradation after contacts metal evaporation as discussed in the previous discussion. The further work would be focused on solving the degradation during the evaporation.

### 3. Conclusions

In conclusion, we succeeded in fabricating close to 20%-efficient IBC silicon solar cells with dopant-free asymmetric MoO<sub>x</sub>/Ag and LiF/Al contacts via simple evaporation process. The thickness of passivating a-Si:H(i) layer and MoO<sub>x</sub> layer was optimized by taking the electrical property and stability into consideration. Furthermore, we employed the Quokka 2 simulation to seek the best condition for cells performance, including the pitch sizes of the back electrodes pattern, passivation quality of the both sides contacts and the electrical property of HTL. The perspective efficiency of the cells by simulated results can exceed 22%, proving the great potential for the simple-process efficient silicon solar cells.

## 4. Experiments

### 4.1. Contact and passivation measurement

Single-side polished n-type c-Si wafers with resistivity of 1–3 Ωcm were used for ETL contact resistivities measurement and single-side polished p-type c-Si wafers with resistivity of 1 Ωcm were used for HTL contact resistivities measurement. The contact resistivities were extracted using the Cox and Strack method. After standard RCA cleaning and dilute hydrofluoric acid (HF, ~2% concentration) dipping, c-Si wafers were deposited with single-side a-Si:H(i) layer by PECVD. HTL (MoO<sub>x</sub>/Ag) and ETL (LiF/Al) with different diameters were thermally evaporated on the a-Si:H(i) layer with thickness of 8 nm/300 nm for HTL and 1 nm/300 nm for ETL without breaking vacuum, respectively, through a shadow mask. The MoO<sub>x</sub> and LiF layers were both processed in the evaporator by a deposition rate of 0.2 Å/s at a base pressure 1.0 × 10<sup>-7</sup> Torr. For a-Si:H(i) passivated samples, a-Si:H(i) layers with different thicknesses were deposited on the both sides by PECVD. Double-side polished n-type c-Si wafers with resistivity of 1–3 Ωcm and thickness of 250 μm were used for passivation characterization. Following standard RCA cleaning and dilute HF dipping, a-Si:H(i) layers with were deposited symmetrically on the both sides of the wafers by PECVD. HTL (8 nm MoO<sub>x</sub>/100 nm Ag) and ETL (8 nm LiF/100 nm Al) with full area were thermally deposited on the silicon substrates to be

used for PL test.

### 4.2. Solar cell fabrication

The IBC solar cells with dopant-free asymmetric hetero-contacts were fabricated using n-type (100)-oriented c-Si wafers (Cz, 200 μm thickness, and 1.0 Ωcm resistivity) here. Before front side passivating and antireflective PECVD SiN<sub>x</sub> layer deposition, the wafers were immersed in tetramethylammonium hydroxide (TMAH), isopropyl alcohol (IPA), and deionized (DI) water mixed solution at 85 °C for 20 min to fabricate single-side randomly pyramidal structure for light trapping. After texturing, the wafers were cleaned with standard RCA process and 75 nm SiN<sub>x</sub> antireflection layers were then deposited on the textured surface by PECVD. For the rear side, a-Si:H(i) passivating layer with the thickness of 5 nm was deposited by PECVD and followed by HTL and ETL evaporation. HTL (8 nm MoO<sub>x</sub>/100 nm Ag) and ETL (1 nm LiF/100 nm Al) were thermally evaporated which were patterned by shadow masks.

### 4.3. Characterization

Keithley 2400 source-meter was used to measure the contact resistivity. The effective excess carrier lifetimes of samples were characterized by photoconductance decay (Sinton WCT 120). PL images were captured using an LIS-R1 PL imaging tool from BT imaging. The photovoltaic performance of the c-Si solar cells was characterized by solar simulator (Sinton Instruments) with an Xe arc lamp under standard test conditions (Air-mass 1.5 illumination, 1000 W/m<sup>2</sup>, 25 °C) with home-made test jig. An encapsulated standard reference c-Si solar cells certified by Fraunhofer Callab was used to calibrate the illumination intensity. The quantum efficiency of the solar cells was measured by a quantum efficiency measurement system (QEX10, PV Measurements).

### Declaration of Competing Interest

The authors declare that they have no known competing financial interests or personal relationships that could have appeared to influence the work reported in this paper.

### Acknowledgements

This work was supported by the National Natural Science Foundation of China (11974242, 62034009, and 11834011). The authors wish to thank Dr. Hao Lin from Sun Yat-sen University for the experimental advice and Dr. Josua Stuckelberger from The Australian National University for the valuable discussion. This work has been financially supported by the Australian Renewable Energy Agency (ARENA) and the Australian Centre for Advanced Photovoltaics (ACAP). The access to PECVD deposition tool for a-Si:H(i) layer at the Australian National Fabrication Facility is gratefully acknowledged.

## References

- Allen, T.G., Bullock, J., Yang, X., Javey, A., De Wolf, S., 2019. Passivating contacts for crystalline silicon solar cells. *Nat. Energy* 4 (11), 914–928. <https://doi.org/10.1038/s41560-019-0463-6>.
- Allen, T.G., Bullock, J., Zheng, P., Vaughan, B., Barr, M., Wan, Y., Samundsett, C., Walter, D., Javey, A., Cuevas, A., 2017. Calcium contacts to n-type crystalline silicon solar cells. *Prog. Photovoltaics* 25 (7), 636–644. <https://doi.org/10.1002/pip.v25.710.1002/pip.2838>.
- Almora O., Gerling L.G., Voz C., Alcubilla R., Puigdollers J., Garcia-Belmonte G., 2017. Superior performance of  $V_2O_5$  as hole selective contact over other transition metal oxides in silicon heterojunction solar cells. *Sol. Energy Mater. Sol. Cells* 168, 221–226. <https://doi.org/10.1016/j.solmat.2017.04.042>.
- Battaglia, C., de Nicolás, S.M., De Wolf, S., Yin, X., Zheng, M., Ballif, C., Javey, A., 2014. Silicon heterojunction solar cell with passivated hole selective  $MoO_x$  contact. *Appl. Phys. Lett.* 104 (11), 113902. <https://doi.org/10.1063/1.4868880>.
- Bivour, M., Temmler, J., Steinkemper, H., Hermle, M., 2015. Molybdenum and tungsten oxide: high work function wide band gap contact materials for hole selective contacts of silicon solar cells. *Sol. Energy Mater. Sol. Cells* 142, 34–41. <https://doi.org/10.1016/j.solmat.2015.05.031>.
- Bullock, J., Cuevas, A., Allen, T., Battaglia, C., 2014. Molybdenum oxide  $MoO_x$ : A versatile hole contact for silicon solar cells. *Appl. Phys. Lett.* 105 (23), 232109. <https://doi.org/10.1063/1.4903467>.
- Bullock, J., Wan, Y., Xu, Z., Essig, S., Hettick, M., Wang, H., Ji, W., Boccard, M., Cuevas, A., Ballif, C., Javey, A., 2018. Stable dopant-free asymmetric heterocontact silicon solar cells with efficiencies above 20%. *ACS Energy Lett.* 3 (3), 508–513. <https://doi.org/10.1021/acsenenergylett.7b01279>.
- Bullock, J., Zheng, P., Jeangros, Q., Tosun, M., Hettick, M., Sutter-Fella, C.M., Wan, Y., Allen, T., Yan, D.I., Macdonald, D., De Wolf, S., Hessler-Wyser, A., Cuevas, A., Javey, A., 2016. Lithium fluoride based electron contacts for high efficiency n-type crystalline silicon solar cells. *Adv. Energy Mater.* 6 (14), 1600241. <https://doi.org/10.1002/aenm.201600241>.
- Dréon, J., Jeangros, Q., Cattin, J., Haschke, J., Antognini, L., Ballif, C., Boccard, M., 2020. 23.5%-efficient silicon heterojunction silicon solar cell using molybdenum oxide as hole-selective contact. *Nano Energy* 70, 104495. <https://doi.org/10.1016/j.nanoen.2020.104495>.
- Freitas, F.S., Merlo, R.B., Marques, F.C., Nogueira, A.F., 2014. Hybrid silicon/P3HT solar cells based on an interfacial modification with a molecular thiophene layer. *Phys. Status Solidi A* 211 (11), 2657–2661. <https://doi.org/10.1002/pssa.v211.1110.1002/pssa:201431568>.
- He, J., Wan, Y., Gao, P., Tang, J., Ye, J., 2018. Over 16.7% efficiency organic-silicon heterojunction solar cells with solution-processed dopant-free contacts for both polarities. *Adv. Funct. Mater.* 28 (34), 1802192. <https://doi.org/10.1002/adfm.201802192>.
- Melskens, J., van de Loo, B.W.H., Macco, B., Black, L.E., Smit, S., Kessels, W.M.M., 2018. Passivating contacts for crystalline silicon solar cells: from concepts and materials to prospects. *IEEE J. Photovoltaics* 8 (2), 373–388. <https://doi.org/10.1109/JPHOTOV.2018.2797106>.
- Richter, M.H.A., Glunz, S.W., 2013. Reassessment of the limiting efficiency for crystalline silicon solar cells. *IEEE J. Photovoltaics* 3, 1184–1191. <https://doi.org/10.1109/jphotov.2013.2270351>.
- Tune, D.D., Flavel, B.S., Krupke, R., Shapter, J.G., 2012. Carbon nanotube-silicon solar cells. *Adv. Energy Mater.* 2 (9), 1043–1055. <https://doi.org/10.1002/aenm.201200249>.
- Wan, Y., Bullock, J., Hettick, M., Xu, Z., Samundsett, C., Yan, D.I., Peng, J., Ye, J., Javey, A., Cuevas, A., 2018. Temperature and humidity stable alkali/alkaline-earth metal carbonates as electron heterocontacts for silicon photovoltaics. *Adv. Energy Mater.* 8 (22), 1800743. <https://doi.org/10.1002/aenm.201800743>.
- Wan, Y., Karuturi, S.K., Samundsett, C., Bullock, J., Hettick, M., Yan, D.I., Peng, J., Narangari, P.R., Mokkapatil, S., Tan, H.H., Jagadish, C., Javey, A., Cuevas, A., 2018. Tantalum oxide electron-selective heterocontacts for silicon photovoltaics and photoelectrochemical water reduction. *ACS Energy Lett.* 3 (1), 125–131. <https://doi.org/10.1021/acsenenergylett.7b01153>.
- Wan, Y., McIntosh, K.R., Thomson, A.F., Cuevas, A., 2013. Low surface recombination velocity by low-absorption silicon nitride on c-Si. *IEEE J. Photovoltaics* 3 (1), 554–559. <https://doi.org/10.1109/JPHOTOV.2012.2215014>.
- Wan, Y., Samundsett, C., Bullock, J., Allen, T., Hettick, M., Yan, D.I., Zheng, P., Zhang, X., Cui, J., McKeon, J., Javey, A., Cuevas, A., 2016a. Magnesium fluoride electron-selective contacts for crystalline silicon solar cells. *ACS Appl. Mater. Interfaces* 8 (23), 14671–14677. <https://doi.org/10.1021/acsami.6b03599>.
- Wan, Y., Samundsett, C., Bullock, J., Hettick, M., Allen, T., Yan, D.I., Peng, J., Wu, Y., Cui, J., Javey, A., Cuevas, A., 2017b. Conductive and stable magnesium oxide electron-selective contacts for efficient silicon solar cells. *Adv. Energy Mater.* 7 (5), 1601863. <https://doi.org/10.1002/aenm.201601863>.
- Wan, Y., Samundsett, C., Yan, D.I., Allen, T., Peng, J., Cui, J., Zhang, X., Bullock, J., Cuevas, A., 2016b. A magnesium/amorphous silicon passivating contact for n-type crystalline silicon solar cells. *Appl. Phys. Lett.* 109 (11), 113901. <https://doi.org/10.1063/1.4962960>.
- Wang, J., Lin, H., Wang, Z., Shen, W., Ye, J., Gao, P., 2019. Hard mask processing of 20% efficiency back-contacted silicon solar cells with dopant-free heterojunctions. *Nano Energy* 66, 104116. <https://doi.org/10.1016/j.nanoen.2019.104116>.
- Wu, W., Lin, W., Zhong, S., Paviet-Salomon, B., Despeisse, M., Jeangros, Q., Liang, Z., Boccard, M., Shen, H., Ballif, C., 2020. Dopant-Free Back-Contacted Silicon Solar Cells with an Efficiency of 22.1%. *Phys. Status Solidi RRL* 14 (4), 1900688. <https://doi.org/10.1002/pssr.201900688>.
- Xu, D., Yu, X., Yang, L., Yang, D., 2018. Design and photovoltaic properties of graphene/silicon solar cell. *J. Electron. Mater.* 47 (9), 5025–5032. <https://doi.org/10.1007/s11664-018-6268-8>.
- Yang, X., Aydin, E., Xu, H., Kang, J., Hedhili, M., Liu, W., Wan, Y., Peng, J., Samundsett, C., Cuevas, A., Wolf, S., 2018. Tantalum nitride electron-selective contact for crystalline silicon solar cells. *Adv. Energy Mater.* 8 (20), 1800608. <https://doi.org/10.1002/aenm.201800608>.
- Yang, X., Bi, Q., Ali, H., Davis, K., Schoenfeld, W.V., Weber, K., 2016. High-performance  $TiO_2$ -based electron-selective contacts for crystalline silicon solar cells. *Adv. Mater.* 28 (28), 5891–5897. <https://doi.org/10.1002/adma.201600926>.
- Yang, X., Lin, Y., Liu, J., Liu, W., Bi, Q., Song, X., Kang, J., Xu, F., Xu, L., Hedhili, M.N., Baran, D., Zhang, X., Anthopoulos, T.D., De Wolf, S., 2020a. A highly conductive titanium oxynitride electron-selective contact for efficient photovoltaic devices. *Adv. Mater.* 32 (32), 2002608. <https://doi.org/10.1002/adma.v32.3210.1002/adma.202002608>.
- Yang, X., Liu, W., De Bastiani, M., Allen, T., Kang, J., Xu, H., Aydin, E., Xu, L., Bi, Q., Dang, H., AlHabshi, E., Kotsosov, K., AlSaggaf, A., Gereige, I., Wan, Y., Peng, J., Samundsett, C., Cuevas, A., De Wolf, S., 2019. Dual-function electron-conductive, hole-blocking titanium nitride contacts for efficient silicon solar cells. *Joule* 3 (5), 1314–1327. <https://doi.org/10.1016/j.joule.2019.03.008>.
- Yang, X., Weber, K., Hameiri, Z., De Wolf, S., 2017. Industrially feasible, dopant-free, carrier-selective contacts for high-efficiency silicon solar cells. *Prog. Photovoltaics* 25 (11), 896–904. <https://doi.org/10.1002/pip.v25.1110.1002/pip.2901>.
- Yang, X., Xu, H., Liu, W., Bi, Q., Xu, L., Kang, J., Hedhili, M.N., Sun, B., Zhang, X., De Wolf, S., 2020b. Atomic layer deposition of vanadium oxide as hole-selective contact for crystalline silicon solar cells. *Adv. Electron. Mater.* 6 (8), 2000467. <https://doi.org/10.1002/aelm.202000467>.
- Yoshikawa, K., Kawasaki, H., Yoshida, W., Irie, T., Konishi, K., Nakano, K., Uto, T., Adachi, D., Kanematsu, M., Uzu, H., Yamamoto, K., 2017a. Silicon heterojunction solar cell with interdigitated back contacts for a photoconversion efficiency over 26%. *Nat. Energy* 2, 17032. <https://doi.org/10.1038/nenergy.2017.32>.
- Yoshikawa, K., Yoshida, W., Irie, T., Kawasaki, H., Konishi, K., Ishibashi, H., Asatani, T., Adachi, D., Kanematsu, M., Uzu, H., Yamamoto, K., 2017b. Exceeding conversion efficiency of 26% by heterojunction interdigitated back contact solar cell with thin film Si. *Sol. Energy Mater. Sol. Cells* 173, 37–42. <https://doi.org/10.1016/j.solmat.2017.06.024>.
- Yu, J., Liao, M., Yan, D., Wan, Y., Lin, H., Wang, Z., Gao, P., Zeng, Y., Yan, B., Ye, J., 2019. Activating and optimizing evaporation-processed magnesium oxide passivating contact for silicon solar cells. *Nano Energy* 62, 181–188. <https://doi.org/10.1016/j.nanoen.2019.05.015>.
- Zhong, S., Dreon, J., Jeangros, Q., Aydin, E., De Wolf, S., Fu, F., Boccard, M., Ballif, C., 2020. Mitigating plasmonic absorption losses at rear electrodes in high-efficiency silicon solar cells using dopant-free contact stacks. *Adv. Funct. Mater.* 30 (5), 1907840. <https://doi.org/10.1002/adfm.201907840>.